Detailed microscopic analysis of self-interstitial aggregation in silicon. I. Direct molecular dynamics simulations of aggregation

Sumeet S. Kapur and Talid Sinno*
Department of Chemical and Biomolecular Engineering, University of Pennsylvania, Philadelphia, Pennsylvania 19104, USA
(Received 18 April 2010; published 19 July 2010)

A comprehensive atomistic study of self-interstitial aggregation in crystalline silicon is presented. Here, large-scale parallel molecular dynamics simulations are used to generate time-dependent views into the self-interstitial clustering process, which is important during post-implant damage annealing. The effects of temperature and pressure on the aggregation process are studied in detail and found to generate a variety of qualitatively different interstitial cluster morphologies and growth behavior. In particular, it is found that the self-interstitial aggregation process is strongly affected by hydrostatic pressure. {111}-oriented planar defects are found to be dominant under stress-free or compressive conditions while {113} rodlike and planar defects are preferred under tensile conditions. Moreover, the aggregation pathways for forming the different types of planar defect structures are found to be qualitatively different. In each case, the various cluster morphologies generated in the simulations are found to be in excellent agreement with structures previously predicted from electronic-structure calculations and observed experimentally by electron microscopy. Multiple empirical interatomic potential models were employed and found to generally provide similar results leading to a fairly consistent picture of self-interstitial aggregation. In a companion article, a detailed thermodynamic analysis of various cluster configurations is employed to probe the mechanistic origins of these observations.

DOI: 10.1103/PhysRevB.82.045205 PACS number(s): 61.72.jj, 61.72.Cc

I. INTRODUCTION

The ion-implantation process, which is used to introduce dopants (e.g., boron or phosphorous) into a silicon wafer, results in a highly nonequilibrium distribution of point defects (self-interstitials and vacancies) and their clusters.[1,2] While many of these defects recombine almost instantly, a large supersaturation of self-interstitials is typically left behind because of the net excess atoms present within the lattice following implantation, creating a distribution of interstitial clusters.[1,2] These clusters are now well known to strongly affect the diffusion behavior of the implanted dopant atoms during the subsequent implant damage annealing[3–10] that is required to heal lattice damage and electrically activate dopant atoms. The diffusion effect is commonly referred to as transient-enhanced diffusion, or TED, because of its strongly nonlinear and time-dependent features.[11] Qualitatively, TED is observed because excess self-interstitials effectively increase the mobility of dopant atoms via the "kick-out" mechanism by increasing the fraction of time the latter spend in the mobile interstitial state rather than the immobile substitutional one.

Self-interstitial clusters have been somewhat more difficult to fully characterize than their vacancy-related counterparts, which are commonly found in vacancy-rich Czochralski-grown silicon crystals.[12–16] While the latter tend to form predominantly octahedral structures bounded by {111}-oriented planes and with 50–200 nm length scales,[17,18] self-interstitial clusters have been observed in a variety of different sizes and morphologies. In particular, it has been challenging to connect quantitatively the implantation and annealing conditions to the observed morphologies, several of which may be present simultaneously.[4,5,7,9,19–24] As a result, there have been numerous studies aimed at experimentally and computationally characterizing the structure, thermodynamics, and dynamical evolution of self-interstitial clusters in crystalline silicon.

The ion-implantation group at CNRS,[25] in perhaps the most comprehensive publications on the subject, have summarized much of the phenomenology associated with self-interstitial clusters and TED in silicon. An important contribution of the work in Refs. 25–27 was to unambiguously demonstrate that the supersaturation of self-interstitials present during TED resulted from a complex combination Ostwald ripening of clusters, out-diffusion of self-interstitials to the wafer surface, and a thermodynamic competition between the various possible cluster morphologies. Earlier studies suggested that the sole source of the excess silicon self-interstitials are dissolving {113}-oriented planar defects formed during the post-implant annealing, which first grow to some maximum size then dissolve during annealing to release mobile Si self-interstitials. The work in Refs. 25–27, however, shows that TED is operational even during cluster ripening (growth) and that it is the supersaturation of single self-interstitials in the vicinity of the clusters that is maintained by the Gibbs-Thompson effect which is responsible for TED. Moreover, it was demonstrated that a quantitative description of the ripening dynamics required that several different cluster morphologies be considered, all of which have been observed experimentally in ion-implanted silicon wafers.

A brief overview of observed self-interstitial cluster morphologies in silicon

In the following, we briefly summarize the salient features of the various self-interstitial cluster morphologies that have been observed experimentally to date. It should be emphasized once again that the dominant self-interstitial cluster structure found in a particular sample depends strongly on

the implant type (i.e., silicon or boron ions, electron irradiation), implant energy and dose, and length and temperature of the post-damage anneal. There are two classes of planar defects commonly found in ion-implanted Si; those that lie on planes normal to the ⟨113⟩ directions and those that are normal to ⟨111⟩. These defects are commonly referred to as {113} and {111} defects, respectively, and are often visible simultaneously.[28–33]

The {113} defects have been the subject of intense investigation because of their uniqueness to Si and Ge, as well as the difficulty associated with their complete atomistic characterization. Their atomistic structure was deduced by Takeda,[34] who showed using high-resolution transmission electron microscopy that these defects are comprised of ⟨110⟩-oriented interstitial chains aligned in the {113} habit plane.[31,34] Images taken during the early stages of {113} defect formation indeed show the presence of line interstitial defects (LIDs), which correspond to chains of di-interstitials aligned along the ⟨110⟩ directions.[34–36] LIDs are surrounded by five-, six-, and seven-membered silicon atom rings. It is believed that these LIDs are the building blocks for planar {113} defects.[31,36] Growth of LIDs along ⟨110⟩ is energetically favorable relative to assembly in the {113} plane because of the lack of dangling bonds at the LID ends. As a result, ion-implanted Si samples often exhibit a preponderance of rodlike {113} defect morphology but both the rodlike and planar structures are believed to originate from the same process. One complicating factor in the analysis of {113} defects is that the spacing between LID building blocks is not necessarily regular, leading to nonperiodicity in the {113} plane and a variable interstitial density.[36] The notation /I/, /IO/, /IIO/, etc. is commonly employed to represent the presence (I) and absence (O) of di-interstitial rows in a particular {113} defect. As expected, the formation energetics and interstitial density of a {113} defect are functions of the specific configuration.[28,31,36]

The most common {111} planar defects observed in implanted silicon are the Frank partial dislocation loops (FDL) and the perfect dislocation loops (PDL).[19–21] Both planar defects are surrounded by dislocation loops while the Frank partials also include a stacking-fault comprised of two additional (111) planes of atoms. Under TEM, these defects often appear as either filled (Frank partial) or open (perfect) oval-shaped structures. FDLs are characterized by a dislocation with a [111]-oriented burgers vector while the PDLs possess dislocations with a [110] burgers vector. These defects are acknowledged to be the most energetically stable interstitial aggregates in the limit of large sizes; after long time annealing of post-implanted wafers they are generally the only defects remaining.[25]

Another type of {111}-oriented defect are the so-called {111} rodlike defects (RLDs). These structures are significantly less common than the {113} rods (LIDs) but have been experimentally observed in silicon following irradiation.[29,30] They are characterized by a ⟨110⟩-oriented interstitial chains aligned in the {111} habit plane, surrounded by alternating five- and eight-membered atomic rings. Interestingly, electronic-structure calculations based on density-functional theory (DFT) predict them to be more energetically favorable than the {113}-oriented rods[31,37] and additional factors beyond simple energetic are thought to be responsible for their relative scarcity. These theoretical findings are supported experimentally in Refs. 32 and 33, in which Ge+ ion-implanted silicon samples exhibit a clear transformation of {113} LIDs into {111} rodlike defects before planar {111} structures are observed. The latter are thought to arise directly from the {111} rods. These experiments further suggest that {111} rodlike defects are more energetically favorable than their {113} counterparts.

Finally, we mention briefly {100}-oriented planar defects.[31,38] These defects are comprised of {100} planar arrays of the well-known Humble/Arai[38–41] four-interstitial cluster structure. They are generally not observed in silicon although have been extensively studied in diamond[38] and germanium.[42] Some evidence for their presence in silicon has been gathered following high-dose boron implantation[43] but it is thought that the boron may play an important role in this case and that the observed {100} defects are examples of boron-interstitial clusters, or BICs. Once again, it is not clear why pure {100} interstitial defects are not generally observed during damage annealing of silicon given that DFT calculations show them to be at least as energetically favorable as {113} defects.[31]

The goals of this paper and its companion (Paper II)[44] are to first apply large-scale atomistic simulations based on empirical interatomic potentials in order to directly study the aggregation and growth of self-interstitial clusters under highly supersaturated conditions. Then, we aim to study the thermodynamic properties of individual clusters in order to explain mechanistically the observations in the direct aggregation simulations. We seek to address issues related to how the various cluster morphologies are related, and what the effects of temperature and hydrostatic pressure on these relationships are. These questions are posed with two primary computational approaches. In this paper, direct large-scale molecular dynamics simulations of self-interstitial aggregation are performed under prescribed temperature and stress conditions. These simulations provide a detailed transient view of the aggregation process and the resulting aggregate morphologies as a function of temperature and pressure. The results from the large-scale simulations are analyzed in Paper II by studying the thermodynamics and morphology of single clusters using a computational method that we have recently developed and applied to the characterization of vacancy aggregates.[45] In this approach, the cluster configurations generated by lengthy molecular dynamics (or equivalently Monte Carlo) simulations are sampled periodically to generate a probability distribution for the formation energies. The formation energy distribution function is directly related to the total classical formation free energy of the cluster, and provides a comprehensive view of cluster thermodynamics at finite temperature and stress. In aggregate, the results of both simulation approaches are combined to infer a comprehensive picture for self-interstitial aggregation.

The remainder of this paper is structured as follows. In the following section, we discuss the methodological details of the large-scale direct aggregation simulations. In Sec. III, the results of simulations based on the environment-dependent interatomic potential (EDIP) (Ref. 46) are presented and discussed in detail. Both temperature and pressure

effects are considered. In Sec. IV, additional results are presented using other interatomic potential functions for silicon. These are compared and contrasted to the EDIP results to generate a consistent qualitative picture of the self-interstitial aggregation process. Conclusions are presented in Sec. V. In the companion paper (Paper II), single cluster thermodynamics are probed in detail using techniques for sampling the potential energy landscape associated with the clusters. These calculations provide a detailed mechanistic view of the effects of temperature and pressure on self-interstitial aggregation and suggest possible explanations for experimental observations.

II. SIMULATION METHODOLOGY FOR LARGE-SCALE SIMULATION OF INTERSTITIAL AGGREGATION

A sequence of parallel molecular dynamics (PMD) simulations were performed using large cubic simulation cells consisting of 39 304–1 000 000 silicon lattice atoms along with 216–1000 silicon self-interstitials, initially placed in uniformly spaced tetrahedral positions. While this initialization procedure obviously does not correspond directly to a post-implantation configuration, it does provide a highly supersaturated environment that leads to rapid aggregation. Variations in the initial interstitial positions were not found to provide appreciable effects in the evolution of aggregates, except at extremely short simulation times. The codes and simulation initialization approaches used in these simulations have been adapted from Prasad and Sinno.[47,48]

The empirical EDIP potential[46] was used in most of the simulations discussed below but a subset of the runs also were carried out with the Stillinger-Weber (SW) (Ref. 49) and Tersoff[50] potentials for silicon. Constant atom number, pressure and temperature ensemble (NPT) PMD simulations at various temperatures and pressures were carried for several nanoseconds (3.8–38 ns), using the Parrinello-Rahman method[51] to control pressure, and velocity rescaling to control temperature. NPT simulations were performed with hydrostatic pressures ranging from −3 to +3 GPa and temperatures ranging from 1000 to 1400 K (for the EDIP runs—other temperatures ranges were employed for the SW and Tersoff potentials as discussed later in the paper). The fifth-order Gear predictor-corrector method with time steps of 1.0–3.2 fs was used to integrate the particle trajectories; convergence of the simulation results with respect to the time step size was checked in each case using short test simulations.

During the course of the PMD simulations, the entire system was quenched periodically to the local minimum energy configuration using a conjugate gradient minimization technique[52] and compared to a reference perfect crystal in order to identify the locations of self-interstitials as a function of time. The unambiguous assignment of self-interstitials within a cluster is difficult because of the substantial local lattice distortion that involves many more atoms than the actual number of self-interstitials.[53] An approach introduced previously[54] is used to identify "defective atoms" (DAs) as those that are more than 0.2 Å away from the nearest lattice site in the reference crystal. Once all DAs are identified, they are grouped into clusters based on the Stillinger criterion[55] with a connectivity distance equivalent to the first-nearest-neighbor distance in the perfect silicon lattice. In each cluster, therefore, the total number of self-interstitials, n_I, is known, but the particular atoms that represent these interstitials is not; the self-interstitials are arbitrarily identified as the n_I most displaced atoms. As will be shown, unique assignment of atoms as self-interstitials is not required to analyze cluster morphologies.

III. DIRECT MD SIMULATION OF SELF-INTERSTITIAL AGGREGATION–EDIP RESULTS

Throughout the following discussion of direct aggregation simulations, simulation cells initialized with 216 000 lattice atoms and 1000 self-interstitials were employed unless otherwise noted. Our base case simulation conditions were chosen to be $T=1200$ K and $P=0$ and the PMD run was allowed to evolve up to 19.2 ns. Snapshots of quenched atomic coordinates at several times are shown in Fig. 1. Large, dark (red online) spheres represent self-interstitials as defined in Sec. II, while the small, light (green online) spheres are lattice atoms that are displaced from their ideal (i.e., perfect crystal) positions by more than 0.2 Å. The latter represent a qualitative measure of the strain-field surrounding the self-interstitial clusters. All other atoms are deleted for clarity.

Several interesting features are apparent during the clustering process. First, small three-dimensional (3D) aggregates are quickly formed throughout the simulation domain [Fig. 1(a)]. These clusters grow by ripening (monomer exchange between clusters) and some coalescence due to small cluster mobility at this temperature. Note that at this stage, most of the atoms represent actual self-interstitials; i.e., relatively few atoms beyond the self-interstitials themselves are appreciably displaced from their ideal lattice positions. At time $t\sim 3$ ns [Fig. 1(b)], the largest of the three-dimensional clusters exhibits a rapid morphological transformation into a planar configuration oriented along the {111} directions. At even later times, more of the growing cluster transform to planar configurations and both {111}- and {100}-oriented platelets are observed; Fig. 1(c).

Close-up views of the different platelet configurations generated during the simulation also are shown in Figs. 1(d)–1(g). All three types of {111} defects discussed in Sec. II are observed: {111}-RLD [Fig. 1(d)], a PDL [Fig. 1(e)], and an FDL [Fig. 1(f)]. In each case, the structure of the planar defect is in excellent agreement with previous literature models obtained by interpretation of TEM images.[25,27–31,56] The {100} planar defects [Fig. 1(g)] are also in structural agreement with literature models,[31,38] although as noted earlier, {100} defects are not typically observed in implanted silicon samples.

Note that the atomic displacement field around the planar defects, as defined by the threshold of 0.2 Å, is three-dimensional and is extends in the direction normal to the plane of the defect by an amount similar to the diameter of the loops. It is likely, therefore, that the capture volume is similarly shaped and that the coarsening dynamics of these defects would be best described on the basis of spheres rather

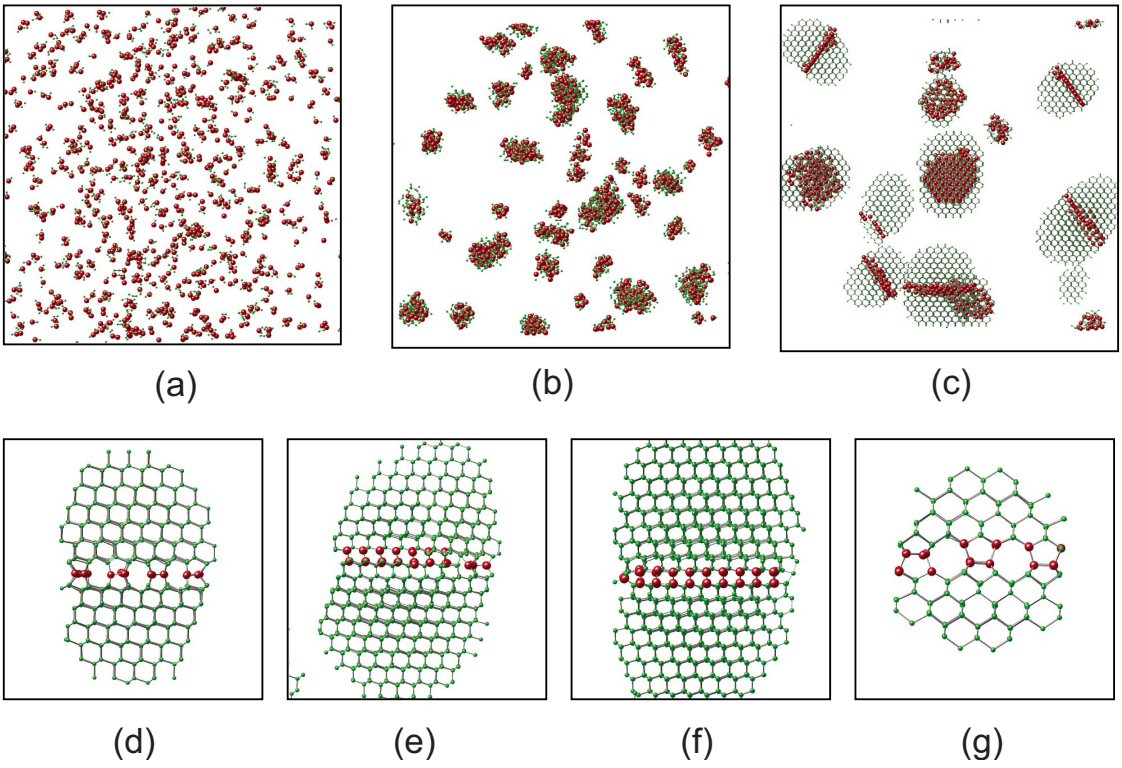

FIG. 1. (Color online) [(a)–(c)] System-wide evolution of interstitial cluster distribution at 1200 K and zero pressure; (a) $t=0.2$ ns, (b) $t=3.7$ ns, and (c) $t=19.2$ ns. Large (red online) spheres denote self-interstitials; small (green online) spheres show lattice atoms that are displaced by more than 0.2 Å from their equilibrium positions. All other atoms are deleted for clarity. [(d)–(g)] Detailed view of cluster structures; (d) {111} RLD, (e) {111} PDL, (f) {111} FDL, and (g) {100} planar defect. All panels are oriented so that the horizontal direction is [110]. For figures (a)–(c) and (g), vertical direction is [001], for figures (d)–(f) vertical direction is [111].

than two-dimensional plates (2D). Evidence for this type of coarsening behavior has in fact been observed in previous experiments.[20] Generally, the shape of the displacement field around a circular dislocation loop is strongly influenced by the orientation of the Burgers vector.[57,58] For both the FDL and PDL defects, the Burgers vectors have significant components normal to the plane of the loop; these are $a/3\langle 111\rangle$ (i.e., pure edge dislocation) and $a/2\langle 110\rangle$, respectively, where a is the lattice parameter.[59] As a result, substantial displacement in direction normal to the loops is expected. This feature of is also true of the other planar defects observed in silicon, i.e., the {100} and {113} structures, as evidenced by their three-dimensional displacement fields. It should be noted that the displaced-atom labels shown in Fig. 1 (and later figures) only correspond to a threshold displacement magnitude, i.e., these plots do not necessarily capture the overall "shape" of the displacement field (nor its direction), which can be quite complex.[58]

Although the progression is not obvious from the limited number of snapshots shown in Fig. 1, we find direct evidence that the {111}-RLDs generally form first by direct collapse of three-dimensional aggregates and then grow to form FDLs and PDLs. It is also worth mentioning here that no evidence of other common defect structures, particularly {113} defects are not observed at any stage of the evolution under the prescribed conditions.

Additional simulations performed at higher temperatures show that the collapse from three-dimensional to planar defect structures takes place at increasing sizes as the temperature is increased. Shown in Figs. 2 and 3 are snapshots from simulations performed at 1300 K and 1400 K, respectively. At 1300 K, very large FDLs and PDLs are observed at a $t=13.4$ ns while at 1400 K no planar defects are apparent by the time the simulation is terminated at $t=8.0$ ns.

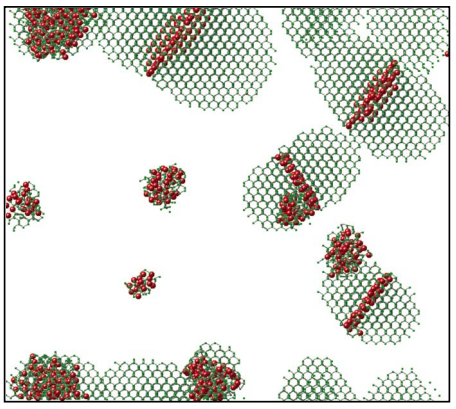

FIG. 2. (Color online) System-wide evolution of interstitial cluster distribution at 1300 K and zero pressure. Total simulation time is 13.4 ns. Large (red) spheres denote self-interstitials; small (green) spheres show lattice atoms that are displaced by more than 0.2 Å from their equilibrium positions. All other atoms are deleted for clarity. Horizontal direction is [110] and vertical [001].

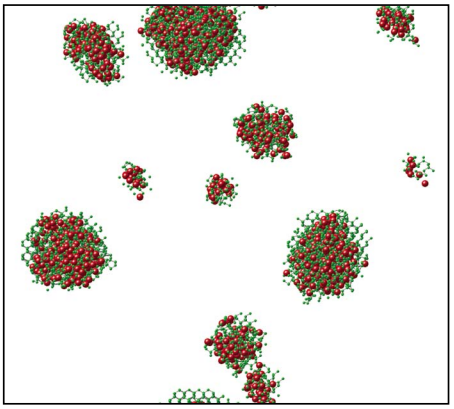

FIG. 3. (Color online) System-wide evolution of interstitial cluster distribution at 1400 K and zero pressure. Total simulation time is 8.0 ns. Large (red) spheres denote self-interstitials, small (green) spheres show lattice atoms that are displaced by more than 0.2 Å from their equilibrium positions. All other atoms are deleted for clarity. Horizontal direction is [110] and vertical [001].

Using the data at several simulation temperatures (1000–1400 K), we can determine approximately the temperature dependence of the transition size at which amorphous three-dimensional structures collapse to any of the planar configurations; see Fig. 4. As will be discussed in more detail in the following section, the morphological transition from three-dimensional to two-dimensional structures is driven by a balance between the high stress and configurational entropy of the three-dimensional aggregates and the relatively low energy of the planar defects. Note that the data in Fig. 4 is approximate because additional interstitials are being incorporated into clusters during the period during which the 3D-2D transition is taking place. Finally, the lack of any {113} defects is notable; these are not predicted to form by the EDIP potential at any temperature in the range investigated. Test simulations with smaller systems at lower temperatures confirm this finding all the way to about 900 K. Even lower temperature simulations were not feasible due to the slow mobility of interstitials.

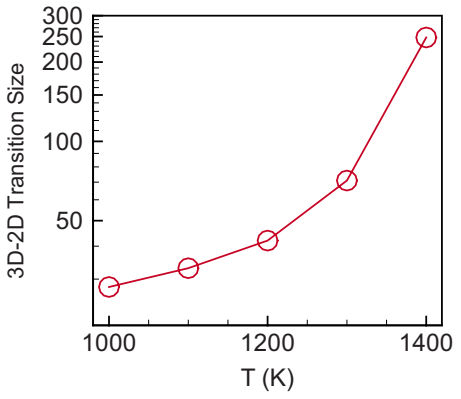

FIG. 4. (Color online) Average number of interstitials in clusters transitioning from three-dimensional to two-dimensional morphology as a function of temperature (zero pressure).

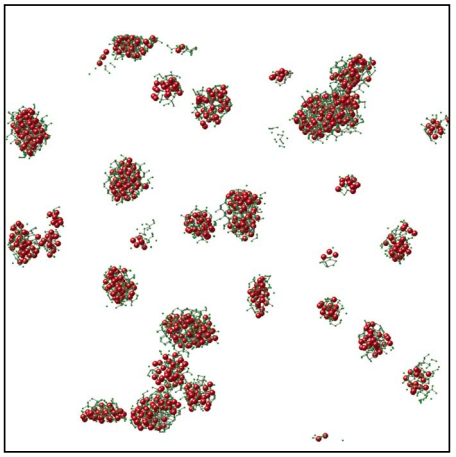

FIG. 5. (Color online) System-wide evolution of interstitial cluster distribution at 1200 K and 3 GPa pressure (approx. 1% compressive strain). Total simulation time is 9.6 ns. Large (red) spheres denote self-interstitials, small (green) spheres show lattice atoms that are displaced by more than 0.2 Å from their equilibrium positions. All other atoms are deleted for clarity. Horizontal direction is [100] and vertical is [001].

A. Effect of hydrostatic pressure on the aggregation behavior of self-interstitials

Next, the effect of hydrostatic pressure on the self-interstitial aggregation behavior was investigated. Although substantial hydrostatic stress is not commonly present in silicon wafer processing, our purpose here is to study the generic influence of stress on defect thermodynamics and aggregation kinetics. Moreover, the transient evolution of the stress state in a wafer during and after ion implantation is not fully understood; literature evidence exists for the presence of both tensile and compressive stresses that evolve in time, and these are strongly coupled to the dose, type and energy of the bombardment.[60–63] Future studies will consider the effects of more complex stress distributions including biaxial and uniaxial fields although some recent atomistic work has addressed the static effects of biaxial and uniaxial stress on individual defects.[64] Further discussion of these results in the context of the present calculations is presented in Paper II.

We begin by considering the effect of hydrostatic compressive stress on self-interstitial clustering at 1200 K. A pressure of +3 GPa was applied to the simulation box, which produces a compressive (uniform) strain of approximately −1% in a perfect EDIP silicon crystal. As shown in Fig. 5, the transformation between three-dimensional and planar defects is essentially inhibited over the time interval (and therefore cluster size) accessed by the PMD simulation (~10 ns). Although the transformation size from three-dimensional to planar morphology is about $n_1 \sim 42$ at 1200 K, several clusters larger than this size are observed to remain in the amorphous three-dimensional state. Otherwise, the three-dimensional aggregates observed under compression are qualitatively similar to those observed at zero stress. It should be emphasized that the shift in the 3D-2D transition to larger sizes is not kinetic in origin. As will be demonstrated in the companion paper (Paper II), the effect of com-

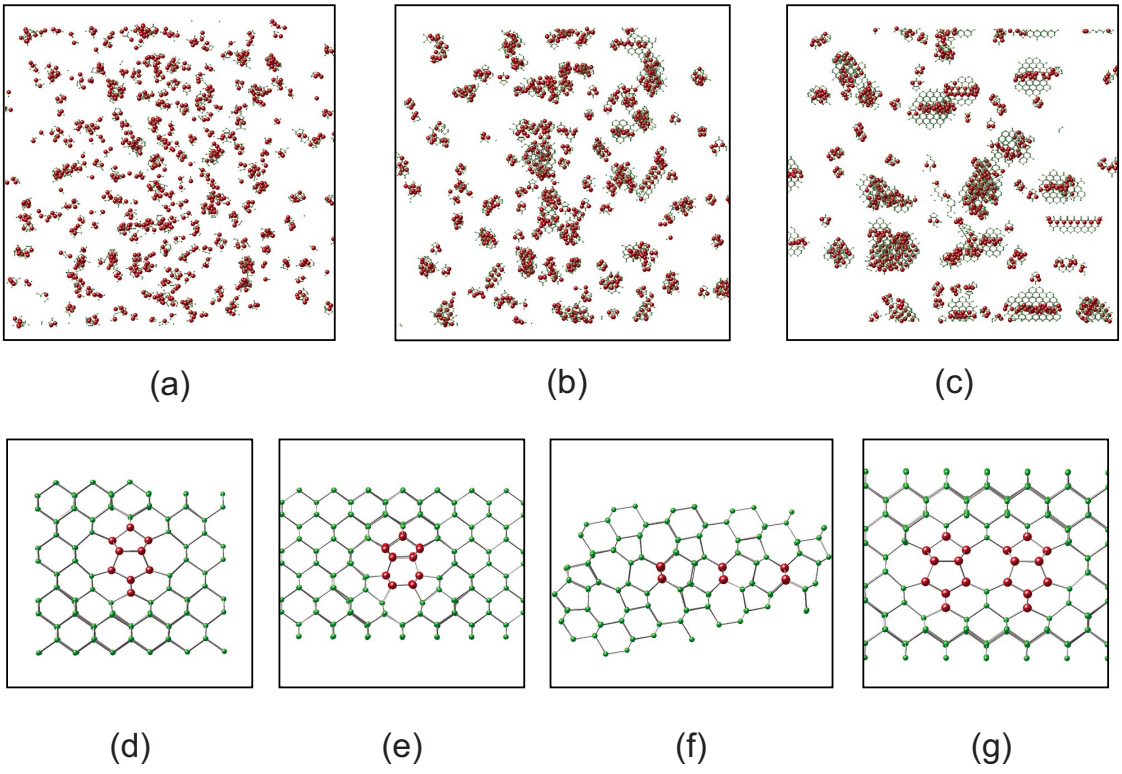

FIG. 6. (Color online) [(a)–(c)] System-wide evolution of interstitial cluster distribution at 1200 K and −3 GPa pressure; (a) $t=0.2$ ns, (b) $t=4.3$ ns, and (c) $t=23.2$ ns. Large (red) spheres denote self-interstitials, small (green) spheres show lattice atoms that are displaced by more than 0.2 Å from their equilibrium positions. All other atoms are deleted for clarity. [(d)–(g)] Detailed view of individual cluster structures; (d) four-intersitial Humble/Arai configuration, (e) partially reconstructed LID, a precursor to {113} defects, (f) {113} planar defect comprised of three ⟨110⟩-oriented interstitial chains (shown), and (g) two Humble/Arai four-interstitial clusters arranged to form a {100} planar defect. All panels except (f) are oriented so that the horizontal direction is [110] and vertical is [001]. In (f), vertical is [113], horizontal is $[\bar{3}\bar{3}2]$.

pression is to increase the configurational entropy associated with the disordered three-dimensional configurations. In other words the inhibition of the 3D-2D transformation is apparently thermodynamic, rather than kinetic, in origin. Further evidence for this hypothesis is provided below in Sec. III B.

The effect of tensile stress on the clustering process is much more profound and complex, as shown in Fig. 6. In this simulation, a tensile hydrostatic pressure of −3 GPa was applied at 1200 K, resulting in a tensile strain of about +1%. Under these conditions, no {111}-oriented defects are observed to form throughout the entire simulation (~23 ns) although some small {100} defects are still formed. Notable qualitative changes relative to the corresponding zero-pressure simulation are that the average cluster size is significantly smaller at all times and that at early and intermediate times [Figs. 6(a) and 6(b)], a large number of four-interstitial complexes are present throughout the simulation domain. Closer inspection of the four-interstitial complexes [Fig. 6(d)] shows that they are exclusively in the well-known cagelike configuration that has been identified as the energetic ground state for the four-intersitial cluster in several previous theoretical studies;[65,66] we henceforth refer to this configuration as the Humble/Arai structure following Refs. 38 and 39.

Most interestingly, several instances of {113} defects and their rodlike precursors (the so-called LIDs) are now found in the simulation. In Fig. 6(e), a partially reconstructed LID structure is shown which is surrounded by five- and seven-membered rings. This structure is a precursor to the (110)-oriented interstitial chains that lead to the formation of {113} defects.[67] An example of the latter is shown in Fig. 6(f), which shows how three of the interstitial chains shown in Fig. 6(e) can aggregate to form a {113} planar defect. Comparison of the {113} defect shown in Fig. 6(f) to literature models indicates that it is of the type /I/, which has the highest density of self-interstitials,[31,68] relative to /IO/ and /IIO/. In the preceding notation, /I/ represents a sequence of adjacent self-interstitial chains while /IO/ and /IIO/ represent sequences in which some chains are missing (a missing chain is denoted by "O"); see Ref. 35 for more details regarding {113} defect classification. The predicted aggregate is in excellent structural agreement with the results of previous calculations and experimentally derived models. Although the formation energies of the various types of {113} defects are slightly different according to previous calculations,[35,36,68,69] it is difficult to extend those conclusions to the present results because the defects formed in the present simulations are finite in size and are likely to be affected by entropic contributions (mainly vibrational). Both of these factors could easily affect the favorability order of the various {113} defect types. Finally, in Fig. 6(g), two Humble/Arai four-interstitial clusters are shown in a side-by-side configuration

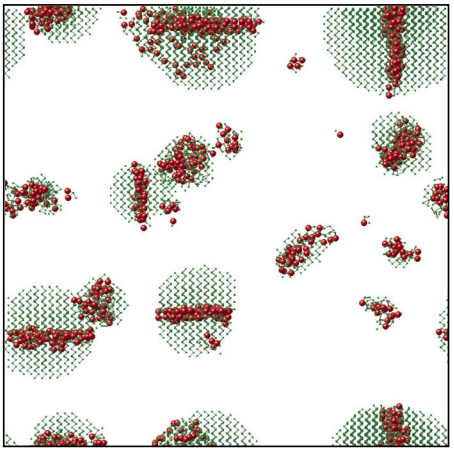

FIG. 7. (Color online) System-wide evolution of interstitial cluster distribution at 1400 K and −3 GPa pressure (approx. 1% tensile strain). Total simulation time is 7.4 ns. Large (red) spheres denote self-interstitials, small (green) spheres show lattice atoms that are displaced by more than 0.2 Å from their equilibrium positions. All other atoms are deleted for clarity. Horizontal direction is [100] and vertical is [001].

(surrounding an eight-membered ring) that represents the building block for {100} planar defects. In other words, {100} planar defects can be found in both zero pressure and tensilely strained simulations while {111} and {113} defects are observed only in the absence and presence of tension, respectively.

The effect of temperature on interstitial aggregation under tensile stress is shown in Fig. 7, which is a snapshot of a system annealed at 1400 K and −3 GPa pressure (1% tensile strain) for 7.4 ns. Now, large {100} platelets are the predominant clusters throughout the simulation domain. It is therefore clear that the formation of {100} defects is somehow more robust than that of {113} defects, at least with respect to elevated temperature. In fact, out of all the defect structures observed in the preceding simulations, {100} planar defects appear under the widest range of operating conditions; for example, they are the only type of defect to exist both at zero pressure and under applied tension. The reasons for this are not obvious from the present simulations but will be addressed with the thermodynamic analysis presented in Paper II.

B. Kinetic considerations for the 3D-2D morphological transformation

The morphological transformation size data in Fig. 4 does not lend insight into the kinetics of transformation between the three-dimensional and planar cluster morphologies. In the following simulation, we probe the transformation kinetics by creating large three-dimensional clusters under +3 GPa compression and 1200 K and then subjecting the system to a rapid decrease in the applied pressure in order to drive the transformation to planar defects. In the results shown in Fig. 8, an MD simulation of self-interstitial aggregation was carried out at 1200 K and +3 GPa for 10.0 ns. No transformation into a planar structure was observed for any cluster as expected due to the compression applied to the system. At 10.0 ns, the simulation box was gradually expanded to remove the compressive stress over a time period of 0.3 ns and the simulation further continued at zero pressure for 6.9 ns. As shown in Fig. 8, clusters larger than $n_I = 42$, which is the critical size at 1200 K (and zero applied pressure), immediately begin to undergo morphological evolution toward the planar {111} configuration [denoted by arrows in Fig. 8(b)]. The speed of the transformation indicates that any kinetic barrier for the collapse is low and that the transition sizes reported in Fig. 4 are equilibrium thermodynamic quantities.

There are two key questions that arise from the preceding results of self-interstitial aggregation as a function of temperature and pressure. The first question is one that is generally associated with the use of empirical potentials: *are the EDIP predictions consistent with those from other commonly employed empirical potentials for silicon such as Tersoff and/or Stillinger-Weber*? In particular, is the strong effect of

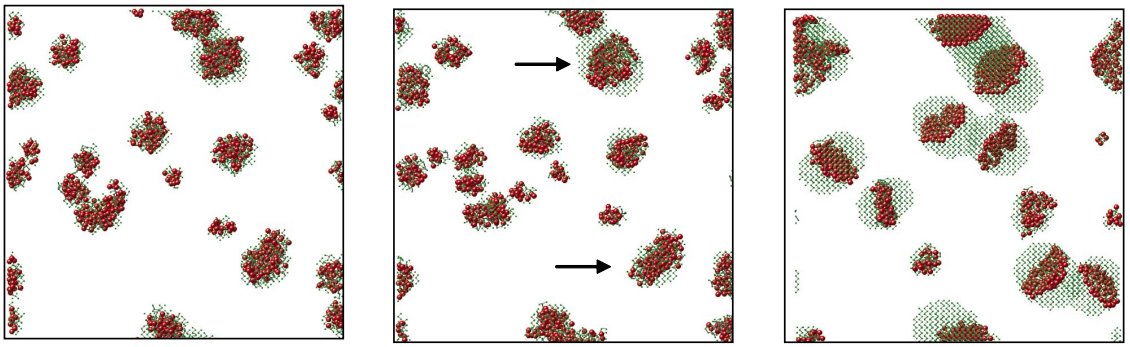

FIG. 8. (Color online) Evolution of self-interstitial clusters during strain relaxation at 1200 K. (a) After 10 ns at +3 GPa, (b) 0.3 ns later as the pressure was reduced from +3 GPa to 0, and (c) after a further 6.9 ns at zero pressure. Large (red) spheres denote self-interstitials, small (green) spheres show lattice atoms that are displaced by more than 0.2 Å from their equilibrium positions. All other atoms are deleted for clarity. Arrows denote onset of 3D-2D transition following pressure drop to zero. For all frames, horizontal direction is [100] and vertical is [001].

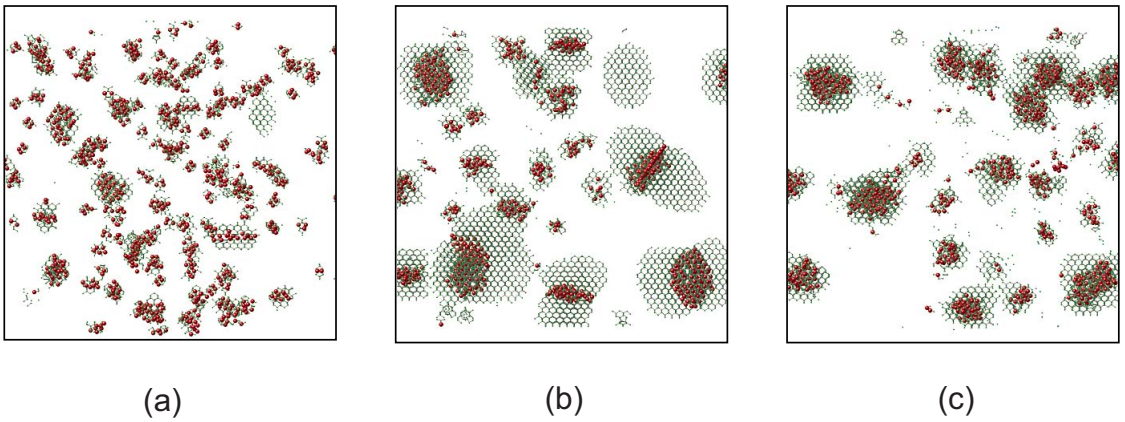

FIG. 9. (Color online) System-wide evolution of interstitial cluster distribution at zero pressure and (a) 1900 K, (b) 2100 K, and (c) 2250 K using the Tersoff potential. Large (red) spheres denote self-interstitials, small (green) spheres show lattice atoms that are displaced by more than 0.2 Å from their equilibrium positions. All other atoms are deleted for clarity. Horizontal direction is [110] and vertical is [001].

hydrostatic pressure (lattice strain) qualitatively reproducible with another potential model or is it a peculiarity of the EDIP potential? We address this question in the following section. The second question is: *precisely what are the mechanistic roles of stress and temperature in the selection of self-interstitial cluster morphology and can our results help explain some of the outstanding questions related to morphological selection in implantation experiments*? This question is addressed in detail in the companion paper (Paper II) by considering in detail the thermodynamics of single clusters under different temperatures and applied pressures.

IV. DIRECT MD SIMULATION OF SELF-INTERSTITIAL AGGREGATION—OTHER POTENTIALS

A. Tersoff potential simulations

Several of the large-scale MD aggregation simulations discussed in the previous section were repeated using the Tersoff potential. Similar cell sizes, self-interstitial concentrations, and applied pressure were used. One well-known limitation of the Tersoff potential for silicon is the very high melting temperature prediction (approx. 2650 K for the parameters given in Ref. 50). The results from the EDIP and Tersoff calculations were thus compared using the ratio of the EDIP and Tersoff melting temperatures, i.e., $T_m^{\mathrm{EDIP}}/T_m^{TERS} \sim 0.58$ so that the temperature interval 1900 K $\leq T \leq$ 2250 K in the Tersoff calculations was approximately mapped onto the interval 1100 K $\leq T \leq$ 1300 K for EDIP. First, a sequence of zero pressure simulations was performed at 1900, 2100, and 2250 K. Snapshots of the atomic distributions at the end of each simulation (total simulated time in each case was approximately 6–7 ns) are shown in Fig. 9.

At 2250K [Fig. 9(c)], the interstitial clusters appear to retain their three-dimensional morphology up to fairly large sizes and do not exhibit a collapse into any type of planar structure during the course of the simulation (the maximum cluster size observed in this simulation is about 90). This result is qualitatively consistent with the EDIP predictions (at 1300K). Unfortunately, shorter Tersoff simulations were necessitated by the fact that the Tersoff potential is computationally more expensive to evaluate than EDIP. However, the Tersoff results at 2100K [Fig. 9(b)] confirm that {111} planar defects are in fact predicted by the Tersoff potential at higher temperatures and the 3D-2D transition size appears to be in line with that predicted by EDIP (see Fig. 4).

A more significant deviation in the predictions of the two potentials appears at 1900 K [Fig. 9(a)]. Here, the Tersoff simulations predict an environment quite similar to that observed under tensile conditions (and moderate temperatures) with EDIP. A large number of four-interstitial clusters in the Humble/Arai configuration are observed, and as expected from the preceding considerations, these are accompanied by the formation of one or two (very small) LID precursors and several small {100}-oriented platelets. Most importantly, no {111}-oriented planar defects are observed by the time the simulation is terminated. In other words, at zero pressure, the Tersoff potential appears to be capable of producing both types of defect morphologies, {111} and {113}/{100}, with variations in the temperature alone. By contrast, tensile conditions were required to stabilize the {113}-related defects within the EDIP simulations. Nonetheless, it is worth noting that all defect configurations obtained with Tersoff are in very good agreement with those predicted in the EDIP simulations, irrespective of the simulation conditions that were employed to obtain them.

In order to establish whether the 1900 K Tersoff results indicate a qualitative discrepancy between the two potentials, which would cast some doubt on the validity of the EDIP predictions discussed above, an additional simulation was performed at 1900 K and +3 GPa of applied pressure; see Fig. 10. As with the EDIP simulations, the interstitial aggregation process is again found to be highly sensitive to hydrostatic pressure. Under compression, {113}-defect precursor LIDs or {100} platelets are no longer generated and almost no Humble/Arai four-interstitial clusters are observed. Although most clusters are still three-dimensional at 6.1 ns, transitions to small {111} platelets are already evident. Qualitatively, at 1900 K and +3 GPa compressive stress the Tersoff potential predicts an environment that is similar to that of EDIP at 1100 K and zero stress while the zero stress Tersoff prediction is roughly consistent with that of EDIP

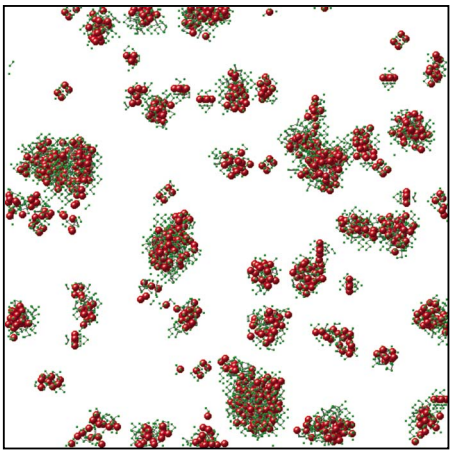

FIG. 10. (Color online) Tersoff simulation at 1900 K and +3 GPa after 6.1 ns of simulation; no two-dimensional structures are present for the current cluster size distribution. Large (red) spheres denote self-interstitials, small (green) spheres show lattice atoms that are displaced by more than 0.2 Å from their equilibrium positions. All other atoms are deleted for clarity. Horizontal direction is [100] and vertical is [001].

under −3 GPa tensile stress. One possibility that has not been addressed directly in our simulations here is that EDIP simulations at zero pressure may indeed also predict the formation of {113} defects but require even lower temperatures than those considered here. However, the reduced mobility of interstitials below about 1000 K makes it difficult to access this regime without substantial computational expense.

B. Stillinger-Weber potential simulations

The SW potential was used to carry out some exploratory simulations to further determine whether the general trends observed with EDIP and Tersoff are reproduced. In Fig. 11, snapshots from smaller simulations (39 304 host particles and 216 self-interstitials) are shown at two different temperatures, 1330 and 1500 K, and pressures, 0 and −3 GPa. A primary reason for employing smaller cells was the additional computational cost associated with evaluating forces with the SW potential. The two temperatures correspond roughly to 1200 K and 1350K, respectively, in the EDIP simulations. In the zero-pressure simulations, clear evidence for the formation of {111} planar defects is apparent with the 1500 K simulation generating a large {111} RLD defect in the center of Fig. 11(b). The application of −3 GPa tensile pressure at 1500 K [Fig. 11(c)] inhibits the formation of {111} defects, and although the system studied is small and the simulation time short, some reorganization into a {100} planar structure is apparent for the defect denoted by the arrow. Again, these trends are qualitatively in agreement with the predictions of the other potentials, demonstrating a remarkable consistency across the three potentials.

V. CONCLUSIONS

The aggregation of silicon self-interstitials into various cluster morphologies has been studied using multiple commonly employed empirical interatomic potentials for silicon. Overall, the different potentials provide a coherent picture for self-interstitial clustering although some differences are apparent. The effects of both temperature and hydrostatic pressure on the self-interstitial aggregation process were considered in the present studies. All three potentials demonstrate similar overall temperature dependence. At high temperature and zero pressure, self-interstitial clusters assume disordered, three-dimensional configurations until they reach large sizes. At lower temperatures, clusters undergo a morphological transition from the three-dimensional state to planar configurations. The critical size for this transition is temperature dependent and becomes smaller as the temperature is decreased, presumably because of reduced entropic favorability of the three-dimensional configurations at low temperatures. Moreover, the transition appears to be kinetically favorable and no apparent barriers are observed in our simulations.

Both the EDIP and SW potentials predict that {111}-oriented planar defects are dominant at zero pressure. The {111} defects are observed in one or more of three configurations: RLDs, FDLs, and PDLs. The structures of the various planar defects predicted in the simulations are in excellent agreement with TEM reconstructions and the results of electronic-structure calculations. Generally, the EDIP simulations show that RLDs form first, followed by FDLs and then PDLs; these trends are consistent with experimental observations. Also seen in the EDIP simulations at zero pressure are {100}-oriented platelike defects, which are not com-

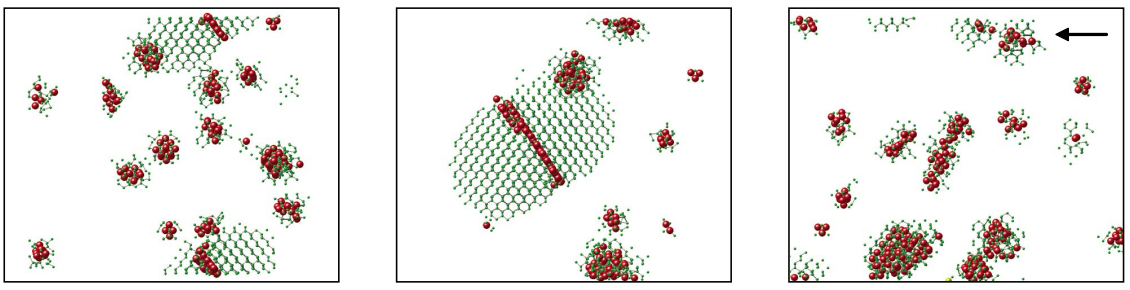

FIG. 11. (Color online) Stillinger-Weber simulations at: (a) 1330 K and zero pressure at 3.3 ns, (b) 1500 K and zero pressure at 2.8 ns, and (c) 1500 K and −3 GPa at 1.9 ns. Horizontal direction is [110] and vertical is [001].

monly observed in real samples, but have been predicted theoretically to be quite favorable relative to other planar defect structures.

A somewhat more complicated picture appears with the Tersoff potential, particularly at lower temperatures. Once again, high temperatures lead to the formation of large three-dimensional clusters, in which the transition to planar morphology is delayed. As the temperature is lowered, {111} planar defects are formed by 3D-2D collapse as seen in the EDIP simulations. However, at the lowest temperature considered (1900 K, or about 1100 K on the EDIP scale), the {111} morphology is no longer observed; instead {100} defects and {113} defect precursors are observed. The latter consist of {110}-oriented interstitial chains that are also commonly observed experimentally in ion-implanted silicon. Associated with this qualitatively different aggregation morphology is a preponderance of four-interstitial clusters with the majority assuming the well-known ground-state "Humble-Arai" configuration.

The apparent difference between the Tersoff and EDIP/SW results can be bridged by considering the effect of hydrostatic pressure on the interstitial aggregation process. In general, it is found that compression, such as temperature, stabilizes the three-dimensional morphology relative to any of the planar structures and shifts the transition size to larger clusters. This is observed for all potentials. However, the application of hydrostatic tension in the EDIP and SW simulations at moderate temperature (1100–1200 K) leads to the disappearance of {111} planar defects and favors the formation of {100} and {113} defects, along with the stabilization of the four-interstitial Humble-Arai clusters. As the temperature is increased under tension, the {113} defects tend to be replaced by large {100} planar defects, which is also observed in the Tersoff case. In other words, it is generally observed that the results of the EDIP and Tersoff calculations are essentially equivalent up to a shift in the applied hydrostatic pressure—a −3 GPa hydrostatic tension environment in the EDIP (and SW) simulations shows similar behavior to the zero-stress Tersoff simulation.

The results in this work suggest an intriguing connection between the stress state of the lattice and the morphology of the self-interstitial defect population, in addition to the expected role of temperature. First, we find that under some conditions, a direct path to the formation of {111} defects is possible, without the previously supposed role of {113} clusters. Here, interstitials aggregate to form three-dimensional structures which spontaneously collapse to form the {111} configurations. Whether this happens or not in the simulations depends strongly on both the temperature and local stress. Under some hydrostatic tension, or at least in the absence of compression (for Tersoff), the formation of {113} defects does indeed appear to be the primary aggregation mode. Under these conditions, previous studies suggest that these defects later transform to {111} structures at larger sizes but the size range for this transformation is beyond the scope of the present simulations. In the next paper, we study the thermodynamics of the various structures obtained here and provide a detailed mechanistic picture for self-interstitial aggregation and its dependence on temperature and hydrostatic stress.

ACKNOWLEDGMENTS

We gratefully acknowledge financial support from the National Science Foundation (Grants No. CTS01-34418 and No. CBET-0730971).

*Corresponding author; talid@seas.upenn.edu

[1] T. Y. Tan, H. Foll, and W. Krakow, Appl. Phys. Lett. **37**, 1102 (1980).
[2] K. S. Jones, S. Prussin, and E. R. Weber, Appl. Phys. A **45**, 1 (1988).
[3] A. Claverie, L. Laanab, C. Bonafos, C. Bergaud, A. Martinez, and D. Mathiotc, Nucl. Instrum. Methods Phys. Res. B **96**, 202 (1995).
[4] P. A. Stolk, H. J. Gossmann, D. J. Eaglesham, D. C. Jacobson, C. S. Rafferty, G. H. Gilmer, M. Jaraíz, J. M. Poate, H. S. Luftman, and T. E. Haynes, J. Appl. Phys. **81**, 6031 (1997).
[5] K. S. Jones, J. Liu, L. Zhang, V. Krishnamoorthy, and R. T. DeHoff, Nucl. Instrum. Methods Phys. Res. B **106**, 227 (1995).
[6] N. E. B. Cowern, H. F. F. Jos, and K. T. F. Janssen, Mater. Sci. Eng., B **4**, 101 (1989).
[7] D. J. Eaglesham, P. A. Stolk, H. J. Gossmann, and J. M. Poate, Appl. Phys. Lett. **65**, 2305 (1994).
[8] B. Colombeau, F. Cristiano, A. Altibelli, C. Bonafos, G. Ben Assayag, and A. Claverie, Appl. Phys. Lett. **78**, 940 (2001).
[9] L. H. Zhang, K. S. Jones, P. H. Chi, and D. S. Simons, Appl. Phys. Lett. **67**, 2025 (1995).
[10] M. J. Caturla, M. D. Johnson, and T. D. de la Rubia, Appl. Phys. Lett. **72**, 2736 (1998).
[11] N. E. B. Cowern, K. T. F. Janssen, and H. F. F. Jos, J. Appl. Phys. **68**, 6191 (1990).
[12] T. Sinno, E. Dornberger, W. von Ammon, R. A. Brown, and F. Dupret, Mater. Sci. Eng. R. **28**, 149 (2000).
[13] T. A. Frewen, T. Sinno, E. Dornberger, R. Hoelzl, W. von Ammon, and H. Bracht, J. Electrochem. Soc. **150**, G673 (2003).
[14] T. A. Frewen, S. S. Kapur, W. Haeckl, W. von Ammon, and T. Sinno, J. Cryst. Growth **279**, 258 (2005).
[15] T. A. Frewen and T. Sinno, Appl. Phys. Lett. **89**, 191903 (2006).
[16] T. Sinno, J. Cryst. Growth **303**, 5 (2007).
[17] M. Itsumi, H. Akiya, T. Ueki, M. Tomita, and M. Yamawaki, J. Appl. Phys. **78**, 5984 (1995).
[18] M. Prasad and T. Sinno, Appl. Phys. Lett. **80**, 1951 (2002).
[19] G. Z. Pan and K. N. Tu, J. Appl. Phys. **82**, 601 (1997).
[20] G. Z. Pan, K. N. Tu, and A. Prussin, J. Appl. Phys. **81**, 78 (1997).
[21] G. Z. Pan, K. N. Tu, and S. Prussin, Appl. Phys. Lett. **71**, 659 (1997).
[22] J. Liu, M. E. Law, and K. S. Jones, Solid-State Electron. **38**, 1305 (1995).
[23] J. Liu, V. Krishnamoorthy, H. J. Gossman, L. Rubin, M. E. Law, and K. S. Jones, J. Appl. Phys. **81**, 1656 (1997).
[24] T. E. Haynes, D. J. Eaglesham, P. A. Stolk, H. J. Gossmann, D.

C. Jacobson, and J. M. Poate, Appl. Phys. Lett. **69**, 1376 (1996).
[25] A. Claverie, B. Colombeau, B. De Mauduit, C. Bonafos, X. Hebras, G. Ben Assayag, and F. Cristiano, Appl. Phys. A **76**, 1025 (2003).
[26] A. Claverie, L. F. Giles, M. Omri, B. de Mauduit, G. Ben Assayag, and D. Mathiot, Nucl. Instrum. Methods Phys. Res. B **147**, 1 (1999).
[27] A. Claverie, B. Colombeau, F. Cristiano, A. Altibelli, and C. Bonafos, Nucl. Instrum. Methods Phys. Res. B **186**, 281 (2002).
[28] C. T. Chou, D. J. H. Cockayne, J. Zou, P. Kringhoj, and C. Jagadish, Phys. Rev. B **52**, 17223 (1995).
[29] L. Fedina, A. Gutakovskii, A. Aseev, J. Van Landuyt, and J. Vanhellemont, Philos. Mag. A **77**, 423 (1998).
[30] L. Fedina, A. Gutakovskii, A. Aseev, J. Van Landuyt, and J. Vanhellemont, Phys. Status Solidi A **171**, 147 (1999).
[31] J. P. Goss, T. A. G. Eberlein, R. Jones, N. Pinho, A. T. Blumenau, T. Frauenheim, P. R. Briddon, and S. Öberg, J. Phys.: Condens. Matter **14**, 12843 (2002).
[32] S. Boninelli, N. Cherkashin, A. Claverie, and F. Cristiano, Appl. Phys. Lett. **89**, 161904 (2006).
[33] S. Boninelli, N. Cherkashin, A. Claverie, and F. Cristiano, Nucl. Instrum. Methods Phys. Res. B **253**, 80 (2006).
[34] S. Takeda, Jpn. J. Appl. Phys., Part 2 **30**, L639 (1991).
[35] M. Kohyama and S. Takeda, Phys. Rev. B **46**, 12305 (1992).
[36] J. Kim, F. Kirchhoff, J. W. Wilkins, and F. S. Khan, Phys. Rev. Lett. **84**, 503 (2000).
[37] J. P. Goss, P. R. Briddon, T. A. G. Eberlein, R. Jones, N. Pinho, A. T. Blumenau, and S. Öberg, Appl. Phys. Lett. **85**, 4633 (2004).
[38] P. Humble, Proc. R. Soc. London **381**, 65 (1982).
[39] N. Arai, S. Takeda, and M. Kohyama, Phys. Rev. Lett. **78**, 4265 (1997).
[40] B. J. Coomer, J. P. Goss, R. Jones, S. Oberg, and P. R. Briddon, J. Phys.: Condens. Matter **13**, L1 (2001).
[41] M. Kohyama and S. Takeda, Phys. Rev. B **60**, 8075 (1999).
[42] S. Muto and S. Takeda, Philos. Mag. Lett. **72**, 99 (1995).
[43] F. Cristiano, N. Cherkashin, X. Hebras, P. Calvo, Y. Lamrani, E. Scheid, B. de Mauduit, B. Colombeau, W. Lerch, S. Paul, and A. Claverie, Nucl. Instrum. Methods Phys. Res. B **216**, 46 (2004).
[44] S. S. Kapur, A. M. Nieves, and T. Sinno, following paper, Phys. Rev. B **82**, 045206 (2010).
[45] S. S. Kapur, M. Prasad, J. C. Crocker, and T. Sinno, Phys. Rev. B **72**, 014119 (2005).
[46] M. Z. Bazant, E. Kaxiras, and J. F. Justo, Phys. Rev. B **56**, 8542 (1997).
[47] M. Prasad and T. Sinno, Phys. Rev. B **68**, 045207 (2003).
[48] M. Prasad and T. Sinno, Phys. Rev. B **68**, 045206 (2003).
[49] F. H. Stillinger and T. A. Weber, Phys. Rev. B **31**, 5262 (1985).
[50] J. Tersoff, Phys. Rev. B **38**, 9902 (1988).
[51] M. Parrinello and A. Rahman, Phys. Rev. Lett. **45**, 1196 (1980).
[52] J. C. Gilbert and J. Nocedal, SIAM J. Control Optim. **2**, 21 (1992).
[53] A. Bongiorno, L. Colombo, F. Cargnoni, C. Gatti, and M. Rosati, Europhys. Lett. **50**, 608 (2000).
[54] S. S. Kapur, M. Prasad, and T. Sinno, Phys. Rev. B **69**, 155214 (2004).
[55] F. H. Stillinger, J. Chem. Phys. **38**, 1486 (1963).
[56] D. Hull and D. J. Bacon, *Introduction to Dislocations* (Pergamon Press, Oxford, 1984).
[57] T. A. Khraishi, J. P. Hirth, H. M. Zbib, and M. A. Khaleel, Int. J. Eng. Sci. **38**, 251 (2000).
[58] S. M. Ohr, J. Appl. Phys. **49**, 4953 (1978).
[59] F. Cristiano, B. Colombeau, C. Bonafos, A. Altibelli, G. Benassayag, and A. Claverie, Solid State Phenom. **82-84**, 201 (2002).
[60] T. Emoto, J. Ghatak, P. V. Satyam, and K. Akimoto, J. Appl. Phys. **106**, 043516 (2009).
[61] G. Bai and M. A. Nicolet, J. Appl. Phys. **70**, 649 (1991).
[62] G. Bai and M. A. Nicolet, J. Appl. Phys. **70**, 3551 (1991).
[63] C. Prunier, E. Ligeon, A. Bourret, A. C. Chami, and J. C. Oberlin, Nucl. Instrum. Methods Phys. Res. B **17**, 227 (1986).
[64] R. J. Bondi, S. Lee, and G. S. Hwang, Phys. Rev. B **79**, 104106 (2009).
[65] S. Birner, J. Kim, D. A. Richie, J. W. Wilkins, A. F. Voter, and T. Lenosky, Solid State Commun. **120**, 279 (2001).
[66] S. Lee and G. S. Hwang, Phys. Rev. B **77**, 085210 (2008).
[67] S. Takeda, Microsc. Res. Tech. **40**, 313 (1998).
[68] J. N. Kim, J. W. Wilkins, F. S. Khan, and A. Canning, Phys. Rev. B **55**, 16186 (1997).
[69] M. Kohyama and S. Takeda, Phys. Rev. B **51**, 13111 (1995).